Transportation Geotechnics 62 (2026) 102129

Contents lists available at ScienceDirect

Transportation Geotechnics

journal homepage: www.elsevier.com/locate/trgeo

Original article

Active MASW for railway ballast characterization in a metro tunnel: A field study in the Milano Metro Line

Valerio Maugeri [a,*], Luca Martinelli [a], Marco Acquati [b], Cristina Jommi [a,c]

[a] Department of Civil and Environmental Engineering, Politecnico di Milano, Piazza Leonardo Da Vinci, 32, Milano, 20133, Italy
[b] MM S.p.A., via del Vecchio Politecnico, 8, Milano, 20121, Italy
[c] Department of Geoscience and Engineering, Delft University of Technology, Stevinweg, 1, Delft, 2628 CN, the Netherlands

ARTICLE INFO

Keywords:
Ballast
Active MASW
Shear-wave velocity
Railway tunnel

ABSTRACT

Reliable estimates of the small-strain stiffness of railway ballast are essential for modeling train-induced vibration transmission and supporting condition assessment in underground railways. This paper presents a Multichannel Analysis of Surface Waves campaign performed inside a tunnel of Milan Metro Line M1, using a controlled impact source, a setting not yet discussed in the literature. A short, densely sampled receiver array was installed along the track, Rayleigh-wave dispersion was obtained in the frequency-phase velocity domain using a phase-shift approach, and a 1-D layered shear-wave velocity V_s profile was obtained by inversion.

A key methodological insight derives from repeating the survey under two track boundary conditions: fastened and unfastened rails. Comparison of dispersion images and inverted profiles shows that the fastened configuration yields higher phase velocities and V_s values, consistent with stronger rail-sleeper coupling and rail-guided energy, which can bias interpretation of ballast properties. Conversely, unfastening the rails suppresses these effects and produces lower misfits and V_s profiles more representative of the ballast-invert-subgrade system.

Three progressively constrained inversion parameterizations were tested to address non-uniqueness and robustness of the obtained profiles. The results confirm that Rayleigh-wave dispersion is primarily controlled by V_s, whereas other characteristics remain weakly correlated. Finally, in-situ stiffness trends of ballast are benchmarked against a laboratory dataset on comparable materials, supporting the plausibility of the velocity profiles obtained.

Overall, the study demonstrates the feasibility of active MASW in a tunnel environment and delivers an operational workflow to obtain ballast-scale V_s profiles, while highlighting the importance of controlling track boundary conditions.

Introduction

Railway infrastructure heavily relies on the mechanical and dynamic performance of the track substructure, where ballast plays a critical role in ensuring the overall track stability, load distribution, and vibration attenuation. As traffic volumes increase, so does the demand on ballast layers, making their continuous monitoring and characterization essential for predictive maintenance and performance optimization.

In underground railways, the relevance of the trackbed mechanical properties is further amplified by the environmental sensitivity to ground-borne vibration, historically recognized as a major issue for metro lines in tunnels [1]. The transmission path from the wheel–rail excitation to the free-field or nearby buildings depends on the dynamic interaction between track components and the supporting ground, and prediction frameworks explicitly require realistic trackbed stiffness inputs [2]. Therefore, reliable estimates of ballast stiffness and damping are not only a material-characterization objective, but a practical prerequisite for vibration prediction and mitigation in urban environment.

Ballast properties evolve with time due to degradation mechanisms driven by repeated loading: particle rearrangement, abrasion and breakage, and the progressive generation/accumulation of fines (fouling). This evolution affects drainage and sleeper stability and accelerates track geometry deterioration, especially under unfavorable moisture conditions [3]. From a mechanical perspective, degradation modifies the granular contact network and can change both stiffness- and damping-related parameters. For instance, increasing fouling has been reported to exacerbate sleeper settlement while reducing the

* Corresponding author.
E-mail address: valerio.maugeri@polimi.it (V. Maugeri).

https://doi.org/10.1016/j.trgeo.2026.102129
Received 25 March 2026; Received in revised form 12 May 2026; Accepted 23 May 2026
Available online 30 May 2026

resilient modulus under cyclic loading [4]. Reduction in damping with ballast degradation has also been reported in laboratory drop-weight impact testing studies [5]. In addition to degradation-state dependence, the vibration attenuation performance of a ballasted trackbed is frequency dependent: vibration laboratory experiments indicate higher damping in a low-frequency range (below ~250 Hz) than at higher frequencies (above ~250 Hz) [6]. At track level, support-stiffness variations and geometry irregularities can increase vehicle–track interaction forces, with implications for vibration generation, ride comfort and fatigue of the components [7]. A report by Zuada Coelho [8] has linked track degradation states to increased vibration generation at transition zones, meaning track sections characterized by abrupt changes in support stiffness.

From an asset-management viewpoint, ballast degradation has clear operational consequences: tamping (the maintenance operation in which the track is lifted and ballast is recompacted beneath the sleepers to restore alignment and level) is the most common action to restore track geometry, yet it must be repeated as geometry degrades, and maintenance demand can become more frequent under adverse substructure conditions [9]. Recent studies and models for tamping demand explicitly show that environmental and ballast-state factors (e.g., moisture and fouling) can markedly increase tamping frequency, i.e., shorten effective maintenance intervals [10]. These links between degradation, dynamic response, and maintenance motivate robust in-situ indicators of ballast condition and stiffness.

Due to the large particle size of ballast, traditional small-scale laboratory tests often fail to reproduce realistic mechanical behavior. As such, large-scale testing has been widely adopted to capture the actual response under load. Among these, large-scale triaxial and box tests are extensively used to investigate ballast behavior under monotonic and cyclic loading conditions. These tests allow researchers to assess key mechanical parameters under different confining pressures, fouling conditions, and ballast grain dimensions. For instance, Anderson and Fair [11] and Suiker et al. [12] reported how ballast compacted under cyclic loads shows significant changes in both stiffness and strength, largely governed by particle rearrangement and breakage mechanisms. Similarly, the studies by Lackenby et al. [13] emphasize the influence of confining pressure in mitigating ballast degradation, identifying optimal pressure ranges that reduce volumetric dilation and particle crushing under high deviatoric stresses. A major aspect in the dynamic behavior of ballast is its stiffness at small strains; this is vital in addressing ground-borne vibrations and noise generation. Both laboratory and field methods have been adopted to evaluate ballast dynamic stiffness, demonstrating the importance of integrating these approaches to bridge the gap between controlled and in-situ conditions. In the context of fouled ballast, experimental evidence confirms that the presence of fine particles severely affects material stiffness [14,15]. Fouling can reduce inter-particle contact efficiency, leading to lower stiffness values, especially at low confining pressures.

To complement the insights gained from large-scale laboratory testing, several seismic-based methods have been developed and increasingly employed in the field to evaluate the mechanical properties of railway substructures, including ballast. These geophysical techniques offer a non-destructive means to assess stiffness parameters, such as shear modulus and derived shear wave velocity, directly in situ, thereby enabling monitoring under actual boundary conditions. Indeed, the dynamic shear modulus G_0 can be computed from density ρ and shear-wave velocity V_s as

$$G_0 = \rho V_s^2. \quad (1)$$

Among the different seismic approaches, surface wave-based methods such as Spectral Analysis of Surface Waves (SASW), Multichannel Analysis of Surface Waves (MASW), and Continuous Surface Waves (CSW) are particularly effective in estimating small-strain stiffness profiles with depth. These methods rely on the dispersive nature of surface waves propagating through layered media, which are sensitive to variations in stiffness across the substructure. By inverting measured dispersion curves, shear-wave velocity profiles can be obtained and subsequently used to assess dynamic moduli of the ballast and underlying layers.

MASW can be implemented either in an *active* configuration, where the wavefield is generated by a controlled impact source, or in a *passive* configuration, where dispersion is extracted from ambient vibrations (traffic, machinery, microtremors) [16]. This distinction is especially relevant in constrained railway environments: controlled excitation can improve repeatability and bandwidth control, while passive recordings can be attractive where active sources are impractical or operational constraints are severe.

Recent railway-oriented studies have demonstrated the practical relevance of these techniques, mostly in *open-air track* conditions or in controlled *model tracks*. For example, MASW surveys by Anbazhagan et al. [17,18] were conducted both on a large-scale laboratory model track (sections with controlled fouling) and on field tracks to characterize ballast and track subsurface layers. A harmonic wavelet transform approach [19] was applied along a high-speed railway line on two bridges, under the practical constraints imposed by sleeper spacing and environmental noise, to retrieve 1-D and 2-D V_s information for the ballast layer. Other field approaches have also been explored: De Bold et al. [20] employed an impulse-response methodology (instrumented hammer and geophone) on a railway model track to relate frequency-domain transfer functions to fouling metrics. Kang et al. [21] investigated shear-wave velocity sensitivity to ballast degradation using a modified bender-element system in laboratory box tests.

Despite this growing body of work, surface-wave testing in railway engineering has been performed either on field open tracks or laboratory model tracks. Applications explicitly addressing underground railways have considered sites close to metro lines in *passive* MASW configurations [22], rather than executing controlled *active* MASW surveys within the tunnel environment itself. Consequently, active MASW case histories on ballast-scale targets inside operational metro tunnels remain essentially absent from the literature.

A further complexity is that MASW inversion is a strongly ill-posed problem, affected by pronounced solution non-uniqueness: multiple, substantially different V_s profiles can fit the same experimental dispersion data within comparable misfit (error) levels. Therefore, credible results require a carefully designed parameterization (layering, bounds, and a-priori constraints) and an explicit assessment of the model.

This paper thus focuses on transferring an active MASW workflow to a metro-tunnel setting and on discussing the practical implications of tunnel geometry, track-structure boundary conditions, usable frequency bandwidth, and inversion robustness. The inversion strategy is supported by a parameterization based on a set of large-scale laboratory results (reported here only synthetically), whose role is to constrain the expected geometrical and mechanical parameters to validated ranges.

Laboratory reference dataset

A large-scale laboratory campaign is used as a reference information to benchmark the MASW estimates and to support a physically plausible parameterization of the inversion problem. The tests were performed at ZAG (Slovenian National Building and Civil Engineering Institute) using a laminar shear box, in which cyclic simple shear (CSS) loading was alternated with impact-generated shear-wave measurements to quantify ballast small-strain stiffness under controlled stress states and degradation conditions. The specimen was instrumented with two embedded unidirectional accelerometers to measure shear-wave travel times across the sample height. Dynamic measurements were performed at the end of each cyclic loading phase by applying three impacts on each of the four lateral faces (12 impacts per phase). The measured shear-wave velocity V_s was then directly related to the small-strain shear stiffness through Eq. (1).

Table 1
Loading pattern for Fresh Ballast (FB) and Fresh-Fouled Ballast (FFB).

Phase	Control	Rate (kPa/s or %strain/s)	Amplitude (kPa or %strain)	σ_v (kPa)	FB cycles	FFB cycles
I	–	–	–	0	–	–
C1	Force	3.13	10	0–10	–	–
CSS1	Force	2.00	±0.9	10	142	202
CSS2	Force	0.20	±7	10	32	37
CSS3	Displacement	0.26	±2	10	91	40
CSS4	Displacement	0.13	±2	10	37	38
C2	Force	3.13	10	10–20	–	–
CSS5	Displacement	0.26	±2	20	44	44
CSS6	Displacement	0.13	±2	20	20	20
CSS7	Force	2.00	±0.9	20	7	14
F	–	3.13	–20	20–0	–	–

Table 2
Loading pattern for Abraded Ballast (AB) and Abraded-Fouled Ballast (AFB).

Phase	Control	Rate (kPa/s or %strain/s)	Amp. (kPa or %strain)	σ_v (kPa)	AB cycles	AFB cycles
I	–	–	–	0	–	–
C1	Force	3.13	10	0–10	–	–
CSS1	Force	2.00	±0.9	10	8	59
CSS2	Force	0.20	±7	10	15	40
CSS3	Displacement	0.26	±1	10	9	8
CSS4	Displacement	0.13	±1	10	9	9
C2	Force	3.13	10	10–20	–	–
CSS5	Displacement	0.26	±1	20	10	12
CSS6	D	0.13	±1	20	10	12
CSS7	Force	2.00	±0.9	20	8	6
F	–	3.13	–20	20–0	–	–

Table 3
Average (μ), standard deviation ($\pm\sigma$), and median (m) of shear wave velocity V_s for each phase and material. Units: [m/s].

Phase	AB			AFB			FB			FFB		
	μ [m/s]	$\pm\sigma$ [m/s]	m [m/s]	μ [m/s]	$\pm\sigma$ [m/s]	m [m/s]	μ [m/s]	$\pm\sigma$ [m/s]	m [m/s]	μ [m/s]	$\pm\sigma$ [m/s]	m [m/s]
C1	216.3	37.1	226.1	200.6	13.5	198.0	148.7	46.6	180.7	211.9	27.5	199.6
CSS1	235.0	42.0	255.3	212.3	10.3	212.1	191.0	45.3	184.8	226.4	31.1	233.9
CSS2	233.9	38.7	240.1	190.4	24.7	192.5	205.9	33.4	200.9	207.7	26.8	217.3
CSS3	220.2	31.5	236.2	214.2	18.6	210.3	185.3	37.0	197.3	209.3	31.2	203.3
CSS4	242.8	41.8	251.5	221.3	29.8	224.6	194.1	62.8	217.3	214.2	31.7	212.2
C2	263.6	57.7	291.7	244.0	37.0	245.2	257.3	30.2	271.3	234.6	42.4	238.4
CSS5	259.9	28.2	270.4	259.5	28.9	254.1	275.1	24.0	281.9	253.4	42.0	257.1
CSS6	269.2	27.2	268.2	264.1	45.7	283.1	279.0	31.6	285.9	253.7	37.4	257.8
F	209.5	29.1	206.1	160.3	18.1	161.9	148.0	16.5	148.8	141.2	22.4	138.5

Fig. 1. Position of the MASW test in Milan Metro Line M1.

Four ballast conditions were tested to represent realistic degradation pathways: Fresh Ballast (FB), Fresh-Fouled Ballast (FFB), Abraded Ballast (AB), and Abraded-Fouled Ballast (AFB). FB consists of clean crushed basalt ballast. AB represents a mechanically degraded skeleton obtained by abrasion, characterized by a more heterogeneous particle size distribution and a higher proportion of rounded coarse particles [23]. Fouled conditions (FFB and AFB) were created by introducing an engineered fouling mixture (a controlled fraction of finer particles) into FB and AB specimens, respectively, targeting a fouling percentage of 30% by mass.

The loading sequence is summarized in Tables 1 and 2, which define the stress levels and cyclic history associated with each V_s estimate. In brief, specimens were first vertically compressed to 10 kPa and subjected to multiple CSS phases at constant vertical stress (including both force- and displacement-controlled phases). The vertical stress was then increased to 20 kPa and further CSS phases were applied, followed by a final unloading step.

Shear-wave velocity was computed from impact records using a travel-time approach previously adopted for coarse granular materials in triaxial testing [24]. For each impact, the first arrival was picked on both accelerometer traces to estimate the wave travel time; the propagation distance was taken as the vertical accelerometer spacing, updated at each phase using the measured top-cap settlement. Wave arrivals were identified through an envelope-based criterion using the Hilbert transform [25]. Table 3 reports, for each material and loading phase, summary statistics (mean, standard deviation and median) of

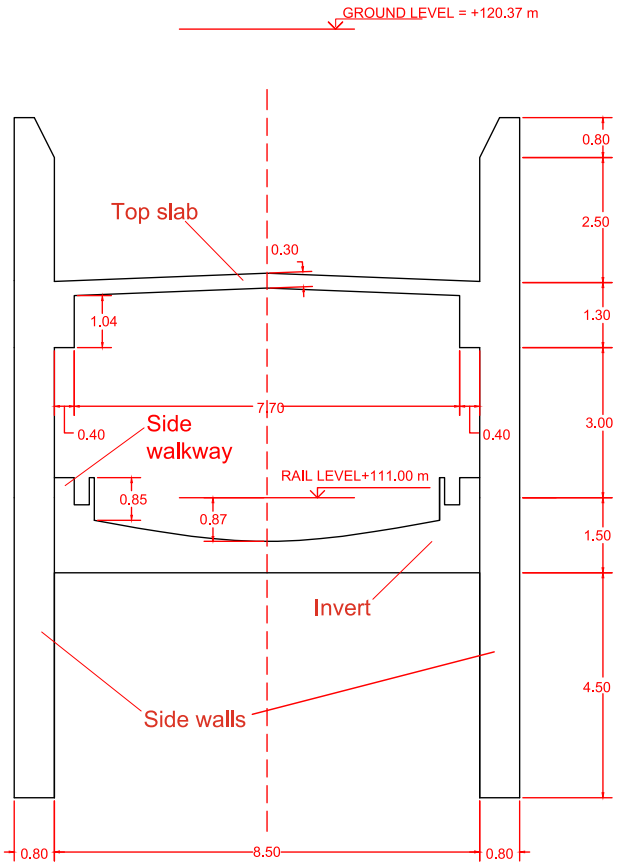

Fig. 2. Investigated cut-and-cover tunnel section. Measures in meters.

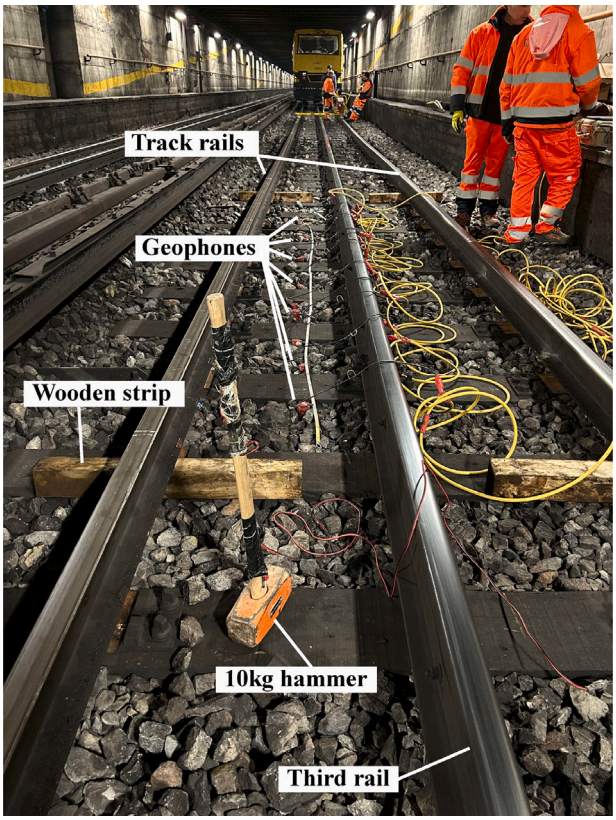

Fig. 3. Configuration of the MASW test.

V_s over the 12 impacts. In summary, the measured shear wave velocities capture the combined effects of fouling, abrasion, and confining stress. Fresh-fouled ballast exhibits higher velocity than fresh ballast at low confinement (10 kPa), while abrasion generally increases the wave velocity unless counteracted by fouling. Under higher vertical stress (20 kPa), differences among materials reduce, with fresh ballast showing a higher wave velocity than its fouled version. The velocity reductions upon unloading confirm the dependency of stiffness on stress state.

In-Situ MASW test

The Multichannel Analysis of Surface Waves (MASW) is a non-destructive seismic technique used to reconstruct the vertical profile of shear wave velocity, by measuring and analyzing the dispersion of surface waves in layered media. Because surface waves are dispersive, different frequencies (wavelengths) sample different depths: higher frequencies are sensitive to shallow layers, whereas lower frequencies probe deeper strata. A standard MASW workflow comprises: (i) extraction of the *experimental dispersion curve* in the frequency–wavenumber (or frequency-phase-velocity) domain; (ii) computation of *theoretical dispersion curves* for parametric subsurface models; and (iii) iterative inversion to identify the V_s profile that best matches observations.

MASW has been successfully applied to characterize ballast and underlying layers, providing indirect measurements of dynamic stiffness and indicators of fouling. Anbazhagan et al. [17,18] demonstrated, using both a full-scale model track and field sections, that the shear-wave velocity of fouled ballast increases with fouling percentage (ratio of the dry weight of material passing through a 9.5 mm sieve to the total dry weight of the sample) up to an optimum fouling point and then decreases beyond it. The reported optimum occurs at about 8% for coal-fouled ballast and about 15% for sandy-clay-fouled ballast. The studies also noted that field V_s tends to exceed model-track V_s for comparable fouling levels; a plausible explanation is the different structural boundary conditions, since in the model-track tests rails and sleepers were not installed, whereas in the field the ballast was constrained by sleepers and rails, with sleepers spaced at about 0.6 m. These results highlight MASW's utility for mapping spatial variations in V_s.

While MASW has been used on open-air tracks and controlled testbeds, to the best of our knowledge and based on the available literature, no MASW surveys have been documented inside a metro tunnel prior to the campaign reported here. Consequently, the implications of tunnel geometry, boundary conditions, usable frequency bandwidth, and inversion parameterization remain under-explored.

The present work addresses this gap by transferring the MASW methodology to a metro-tunnel setting. Commissioned by MM S.p.A., the company that manages the Milan Metro, the campaign was designed to assess the state and potential discontinuities within the ballast beneath the rails. The investigations were carried out on 14 February 2025 near Villa San Giovanni station on the Milan Metro Line M1, as shown in Fig. 1.

Site configuration

The survey was conducted inside a cut-and-cover, box-shaped metro tunnel (Fig. 2) near Villa San Giovanni station in the city of Milan. In this section the tunnel is straight, with uniform cross-section along the measurement line. The track is ballasted with andesite stones. The degree of ballast degradation could not be quantified in this campaign, however, visual observation indicates a fresh and clean ballast surface. In contrast, ballast at depth is plausibly more degraded, since it is likely to include older material that has remained in place since the line was originally built and opened to service in 1964. Based on typical values reported for clean, well-compacted railway ballast, a bulk density on the order of $\rho \approx 1.8\,\mathrm{Mg/m^3}$ may be expected. The ballast

(a) (b)

Fig. 4. Rail unfastening procedure: (a) removal of the fastening bolts; (b) lifting of the rail using a mechanical jack.

layer beneath the measurement line is about 0.50 m thick and rests on a 0.50 m thick reinforced-concrete invert. The section comprises two tracks: one towards Sesto Marelli and one towards Sesto San Giovanni. Each track features a third rail (power supply) located near the track centerline while a fourth rail (power return) runs between the two tracks. The support spacing of the third rail is 4.48 m. Wooden sleepers measure 2.6 m (transverse width) × 0.24 m (longitudinal length) × 0.16 m (height), with 0.64 m spacing, and a mass of approximately 95 kg each. The line is equipped with 50E5 (UNI 50) rails, which are bolted to each sleeper through the fastening system, as shown in Fig. 4(a).

Experimental setup

The MASW measurement line was installed along the track towards Sesto Marelli (Fig. 3). The survey was deliberately repeated under two boundary-condition states: (i) *fastened rails* (in-service track condition) and (ii) *unfastened rails* (track mechanically decoupled from the sleeper system). The objective was to quantify the extent to which the running rails act as a longitudinal waveguide and contaminate the measured Rayleigh-wavefield. To the best of the authors' knowledge, a paired active-MASW comparison on the same track section with rails fastened and unfastened has not been previously reported, and this gap is even more pronounced for rail tracks in tunnel environments, making it a key methodological contribution of the present work.

Unfastening was carried out on the two main running rails by removing the fastening bolts at each sleeper over an extended segment around the measurement line (approximately 10 m upstream and 10 m downstream of the 3.84 m receiver aperture, i.e., the length of the receiver array). The rail foot was then lifted off the rail seats using a mechanical jack (Fig. 4), and continuous wooden strips were inserted beneath the rail foot. These supports were located outside the active MASW spread, approximately 0.30 m before the impact source and 0.30 m after the last receiver, as shown in Fig. 3. This configuration kept the rails slightly raised and mechanically decoupled from the sleepers during the acquisition time, while preserving track alignment and preventing unwanted re-contact during the tests. The procedure effectively interrupts the rail-sleeper load path and substantially reduces along-rail waveguiding. For technical reasons, the third rail could not be unfastened; however, its support spacing is 4.48 m, which exceeds the receiver-array length. In the present layout, the two nearest third-rail supports lie approximately 18 cm upstream and 18 cm downstream of the two ends of the acquisition aperture. Therefore, any third-rail-related guided response is expected to have a limited influence on the wavefield recorded along the receiver array.

Data were acquired with a 48-channel Ambrogeo ECHO-48 seismograph (24-bit sigma–delta A/D) at 1 kHz sampling frequency with a 0.1 s record length. Receivers were vertical 10 Hz geophones (OYO Geospace) equipped with 6 cm steel spikes to anchor securely into the ballast, enhancing ground coupling and reducing sensor rocking. Thirteen geophones were installed at spacing $\Delta x = 0.32$ m, yielding a total array length $L = 3.84$ m (Fig. 5). A near-source trigger geophone synchronized recording at the instant of impact. The impulsive source was a manually operated 10 kg sledgehammer striking a 10 × 10 cm steel plate placed on the ballast surface, with a source-first-receiver offset of 0.32 m along the track. Each track configuration was tested twice, and the resulting dispersion images and inverted profiles showed satisfactory repeatability.

The hammer was not instrumented with a force sensor; therefore, the input force time history and the exact frequency content of each impact were not measured directly. This is potentially a limitation, because the frequency content of the active source controls the usable bandwidth of the surface wave record and, consequently, the range of wavelengths available for dispersion analysis [26]. Nevertheless, the adopted source configuration is consistent with previous active MASW studies using a 10 kg sledgehammer on a metallic plate, which reported usable frequency ranges extending up to about 120–210 Hz [27,28]. Moreover, the phase-shift procedure used to retrieve the dispersion image, described in Section "Dispersion images", relies on phase coherence across the receiver array rather than on absolute amplitudes.

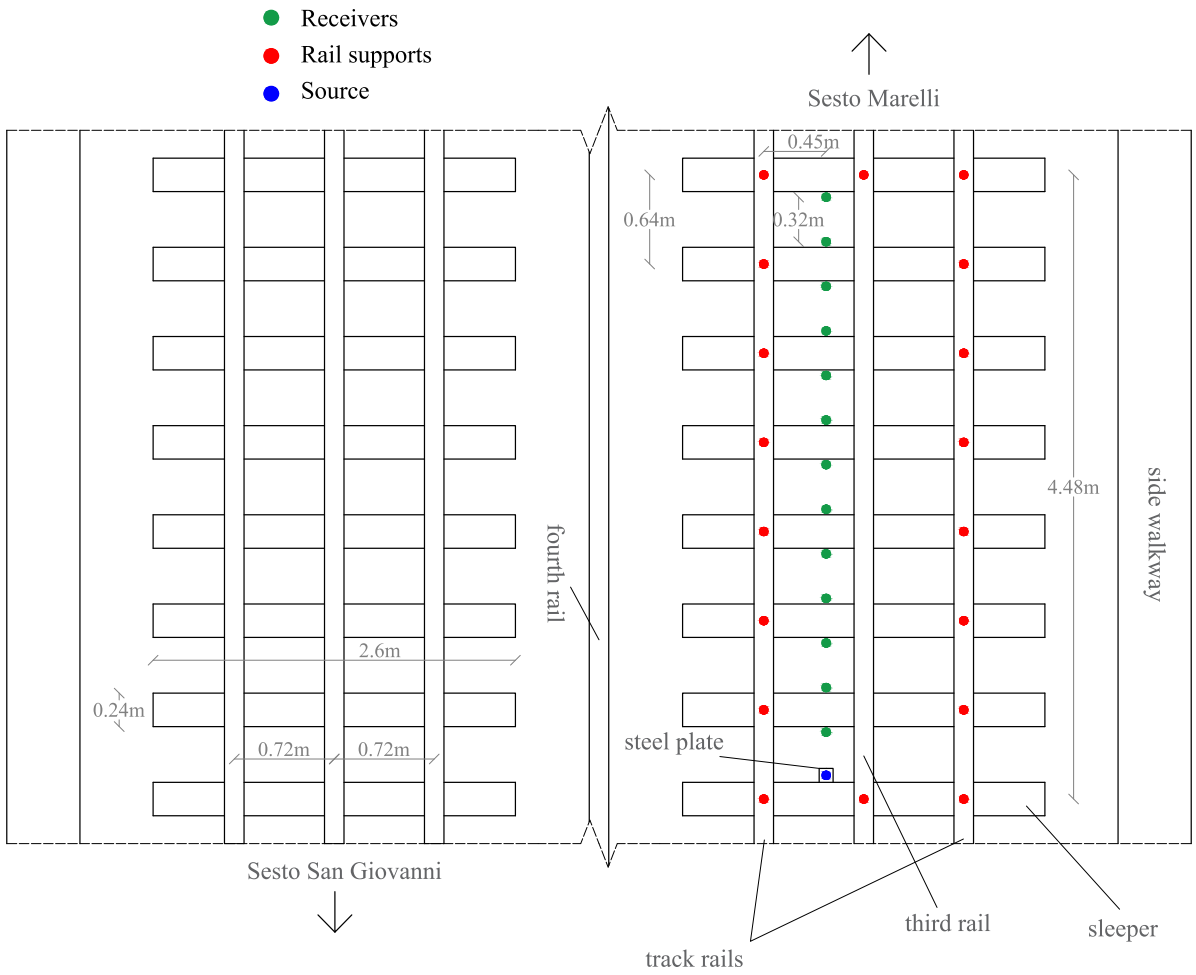

Fig. 5. Plan view of the experimental setup adopted for the MASW test, showing sensors (green dots), rail supports (red dots), and the impact source (blue dot).

Therefore, variations in impact energy are expected to affect signal amplitudes more than the identified phase-velocity trend. To improve repeatability, the same hammer, steel plate, impact position, receiver layout, and acquisition settings were used for all repeated tests.

It is important to note that the experimental setup closely matches the one of Anbazhagan et al. [18], used in the laboratory track. In their model, the ballast sat on a rigid concrete floor, while in the present study the ballast rests on a reinforced-concrete invert; this similarity in boundary conditions makes the Rayleigh-wavefield comparable between studies. A similar dense sampling strategy was also adopted: a tight receiver distance ($\Delta x = 0.32$ m) corresponds to half the sleeper spacing, so that two receivers fall in each sleeper bay, increasing near-field sampling and enabling to increase the resolution within the shallowest ballast layer. Given that the receiver spacing controls the shortest wavelength that can be measured without spatial aliasing, reducing the spacing allows to analyze shorter wavelengths, which govern both the shallowest resolvable depth and the minimum resolvable layer thickness. The receiver spacing is nearly equal to the shortest wavelength, therefore, to the shallowest resolvable depth of investigation [29]. On the other hand, as a rule of thumb, the array length (3.84 m) should be at least equal to the target maximum wavelength, that is approximately twice the intended maximum investigation depth [26,30].

Dispersion images

Figs. 6(a) and 6(b) show the normalized seismic traces for both track configurations. In both cases, the channel nearest to the source was saturated (no oscillations can be observed after the initial spike) and was therefore excluded; for this reason, subsequent processing used the remaining 12 receivers. The analysis was performed with the open-source software package Geopsy and its Dinver inversion module [31].

The dispersion image was computed using the *phase-shift* method. In practice, the recorded seismic traces in the time domain, $u(x_n, t)$, defined at receiver offsets x_n and time t, were transformed to the frequency domain by applying a 1-D Fast Fourier Transform (FFT) to each trace, obtaining the complex spectrum $U(f, x_n)$. For each frequency f, the spectrum at each receiver was normalized by its magnitude to mitigate the effect of geometrical spreading and offset-dependent amplitude variations. The dispersion energy was then mapped in the frequency-phase-velocity plane by scanning trial phase velocities c and summing the phase-shifted spectra over all receivers:

$$A(f,c) = \left| \sum_{n=1}^{N} \frac{U(f,x_n)}{|U(f,x_n)| + \varepsilon} \exp\left(i\, 2\pi f \frac{x_n}{c} \right) \right|, \tag{2}$$

where $U(f, x_n)$ is the complex Fourier spectrum of the nth trace at offset x_n, and ε is a small stabilizing constant. Energy ridges in $A(f, c)$ correspond to phase velocities satisfying phase coherence across the array and therefore delineate the experimental Rayleigh-wave dispersion image [32,33].

The dispersion spectra in Figs. 6(c) and 6(d) also report the spatial-aliasing limit imposed by the receiver spacing Δx. For a regularly sampled array, the maximum unaliased wavenumber is

$$k_{\max} = \frac{\pi}{\Delta x}, \tag{3}$$

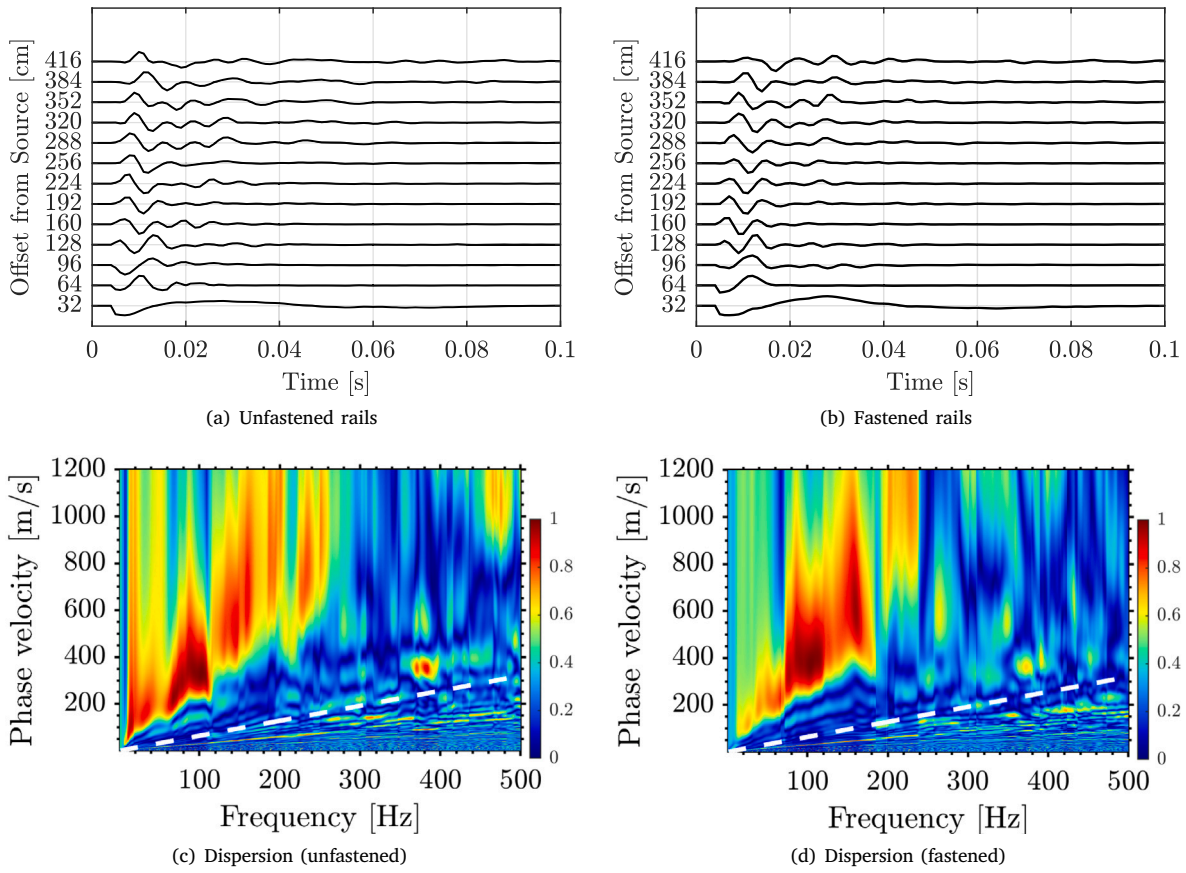

Fig. 6. (Top) Normalized traces; (bottom) phase-shift dispersion images, for unfastened and fastened rails. The spatial-aliasing limit imposed by the receiver spacing Δx is also shown as a white dashed line, defined by $c_{\text{alias}}(f) = 2\,\Delta x\,f$.

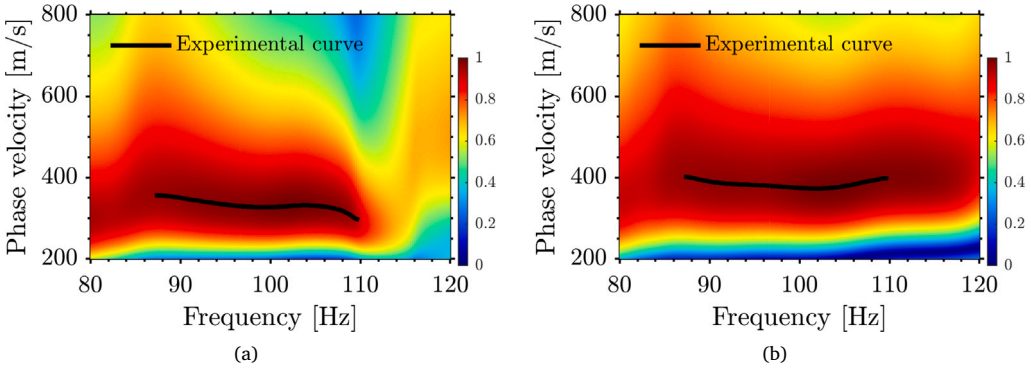

Fig. 7. Picked experimental dispersion curves: (a) unfastened rails; (b) fastened rails.

which corresponds to a minimum resolvable wavelength

$$\lambda_{\min} = 2\Delta x. \tag{4}$$

Using the relation

$$\lambda = \frac{c}{f}, \tag{5}$$

the corresponding aliasing boundary in the frequency-phase-velocity domain is

$$c_{\text{alias}}(f) = 2\,\Delta x\,f. \tag{6}$$

Phase-velocity estimates below this boundary value may be affected by spatial aliasing, because wavelengths shorter than $2\Delta x$ cannot be uniquely represented by the discrete receiver sampling.

The phase-shift approach is particularly suitable for the present tunnel survey because it can produce high-resolution dispersion images even when the record contains a relatively small number of traces and the usable offset range is limited, as is often the case in near-surface investigations and constrained environments. In contrast, more traditional multichannel transforms, such as f–k [34], require wide aperture and a large number of traces to maintain resolving power and to separate modes robustly; when spread length and channel count are limited, their resolution degrades significantly [32].

As shown in Figs. 6(c) and 6(d), the dispersion images obtained with rails unfastened and fastened exhibit markedly different energy distributions. Nevertheless, both cases display a dominant and continuous high-energy band between 80 and 120 Hz, i.e., a frequency

Table 4
Parameterization adopted for inversion. The same scheme is used for rails unfastened (cases 1) and fastened (cases 2).

(a) Case a

Layer	V_s [m/s]	V_p [m/s]	ρ [kg/m^3]	ν [–]	Bottom depth [m]
1	90–300	200–900	1600–3000	0.20–0.40	0.2–0.3
2	90–300	200–900			0.4–0.6
3	2000–3000	1000–5000			0.9–1.1
4	300–3000	200–5000			–

(b) Case b

Layer	V_s [m/s]	V_p [m/s]	ρ [kg/m^3]	ν [–]	Bottom depth [m]
1	90–300	200–900	1600–2100	0.20–0.40	0.2–0.3
2	90–300	200–900	1600–2100		0.4–0.6
3	2000–3000	1000–5000	2300–2600		0.9–1.1
4	300–3000	200–5000	1600–2100		–

(c) Case c

Layer	V_s [m/s]	V_p [m/s]	ρ [kg/m^3]	ν [–]	Bottom depth [m]
1	90–300	200–900	1600–2100	0.20–0.40	0.2–0.3
2	90–300	200–900	1600–2100	0.20–0.40	0.4–0.6
3	2000–3000	1000–5000	2300–2600	0.15–0.25	0.9–1.1
4	300–3000	200–5000	1600–2100	0.20–0.40	–

Table 5
Best layered profiles obtained from MASW inversion. Left column: Case 1a–1c; right column: Case 2a–2c.

(a) Case 1a

Layer	V_s [m/s]	V_p [m/s]	ρ [kg/m^3]	Thickness [m]
1	154.9	316.1	2596	0.22
2	152.1	266.9	2596	0.37
3	2380.9	4108.0	2596	0.40
4	303.0	3055.5	2596	–

(b) Case 2a

Layer	V_s [m/s]	V_p [m/s]	ρ [kg/m^3]	Thickness [m]
1	182.4	378.1	1683	0.23
2	168.5	325.7	1683	0.36
3	2142.7	4404.4	1683	0.32
4	420.8	3275.9	1683	–

(c) Case 1b

Layer	V_s [m/s]	V_p [m/s]	ρ [kg/m^3]	Thickness [m]
1	157.1	303.8	1676	0.22
2	152.5	269.6	1658	0.37
3	2016.3	3468.7	2348	0.35
4	412.5	872.2	2094	–

(d) Case 2b

Layer	V_s [m/s]	V_p [m/s]	ρ [kg/m^3]	Thickness [m]
1	163.5	541.0	1884	0.29
2	189.8	349.2	1667	0.31
3	2000.0	3434.4	2479	0.31
4	412.5	813.5	2016	–

(e) Case 1c

Layer	V_s [m/s]	V_p [m/s]	ρ [kg/m^3]	Thickness [m]
1	148.0	303.8	2089	0.25
2	151.0	264.3	1973	0.31
3	2142.7	3947.7	2506	0.41
4	334.7	2936.3	2055	–

(f) Case 2c

Layer	V_s [m/s]	V_p [m/s]	ρ [kg/m^3]	Thickness [m]
1	161.9	797.4	2033	0.23
2	175.3	294.8	1662	0.33
3	2099.7	3645.7	2328	0.36
4	404.4	4328.5	1813	–

interval where the dispersion ridge is most energetic and traceable across adjacent frequencies. In this frequency range, the fastened configuration consistently yields energy ridges at higher phase velocities. This common high-energy band, in particular 87–110 Hz, was therefore selected for picking of the experimental dispersion curves used in the subsequent inversion.

The experimental dispersion curve was extracted from the phase-shift images (Figs. 7) using an automated picking procedure. Over the selected frequency range (87–110 Hz), the picked phase velocity at each frequency was defined as the value c that maximizes the phase-shift spectrum $A(f, c)$.

MASW inversion

Inversion was carried out in Dinver, the inversion module of the Geopsy software, using the Neighborhood Algorithm (NA) [35,36], a global stochastic search that iteratively proposes layered 1-D models, computes the corresponding theoretical fundamental-mode Rayleigh dispersion curve, and evaluates its fit to the experimental picks through the Geopsy misfit. In Geopsy, the misfit is the root-mean-square difference between experimental and theoretical phase velocities at the picked frequencies, normalized by the phase-velocity values [35]. For each inversion, the algorithm explored 10 000 models and returned the best-fitting ensemble.

A key aspect of the MASW study is that surface-wave inversion is inherently non-unique and ill-posed: different combinations of elastic parameters and layer thicknesses may fit the same experimental dispersion curve within the picking uncertainty, leading to potential interpretation ambiguities [26]. For this reason, rather than adopting a single default setup, for each track configuration we tested three progressively more constrained parameterizations (Cases a–c), reported in Table 4 and explained in the following. In all inversions, the parameterization was built around a consistent and physically plausible

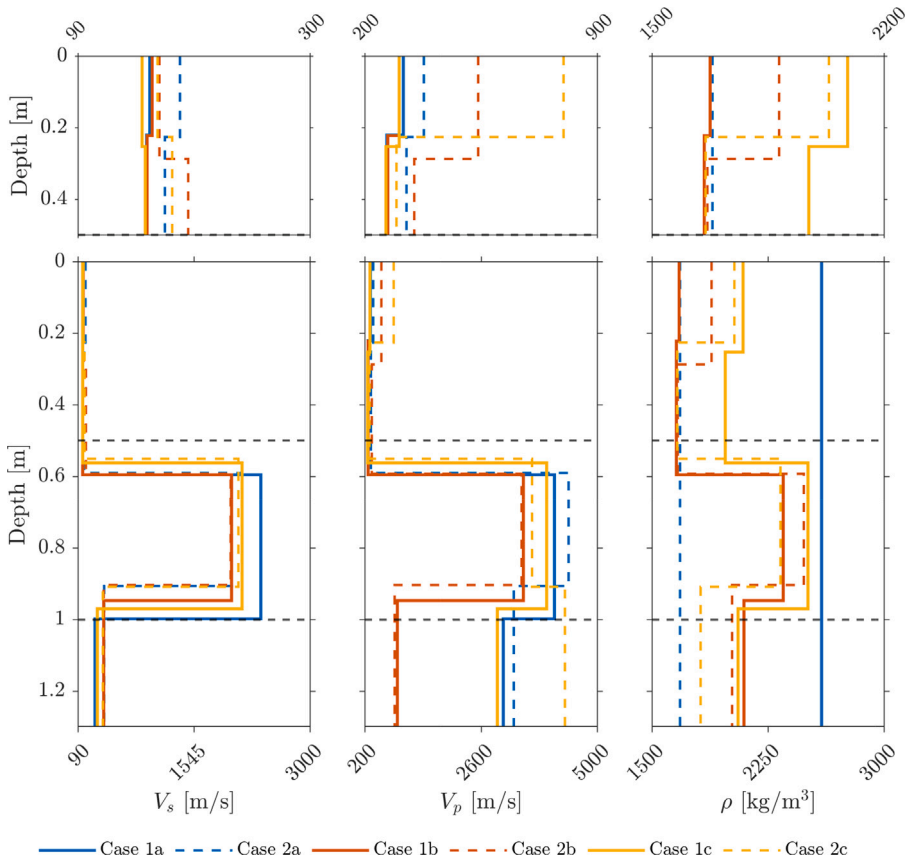

Fig. 8. Best layered profiles obtained from MASW inversion for all cases. The black dashed horizontal lines indicate the ballast-invert and invert-subgrade interfaces expected from the design drawings. A zoomed view, on top of each profile, is included to detail ballast layers.

tunnel-track stratigraphy (two ballast sublayers, reinforced-concrete invert, and underlying soil), compatible with the expected resolution of the acquisition (receiver spacing and array length). The choice of bounds was also informed by the reference laboratory dataset (Section "Laboratory reference dataset"), which provides plausible V_s ranges for ballast under low confinement.

In the inversion module, each layer is defined by independent ranges for S-wave velocity V_s, P-wave velocity V_p, and bulk density ρ, together with a thickness (or bottom depth). In addition, it is allowed to prescribe admissible ranges of Poisson's ratio ν as a consistency constraint: candidate models whose (V_s, V_p) combinations imply ν outside the prescribed bounds are rejected. In an isotropic elastic medium, ν is obtained from V_s and V_p as

$$\nu = \frac{V_p^2 - 2V_s^2}{2\left(V_p^2 - V_s^2\right)}. \tag{7}$$

Importantly, for each level of constrained parameterization (Cases a–c), the same scheme was used for the two track configurations (rails unfastened: Cases 1; rails fastened: Cases 2), so that differences between the resulting profiles can be attributed primarily to changes in the recorded wavefield rather than to inversion settings.

All three parameterizations (Cases a–c) adopt the same 1-D stratigraphic scheme composed of four material layers (Layers 1–3 over a half-space, Layer 4), with uncertain interface depths for Layers 1–3. The overall bounds assigned to the inversion parameters differ across Cases a–c and are summarized in Table 4 (subtables 4a–4c).

The three tested parameterizations (Cases a–c) are intentionally designed to progressively increase prior constraints, moving from global (ρ, ν) bounds (Case a), to a layer-specific density range for the reinforced-concrete invert (Case b), and finally to layer-dependent ranges for both ρ and ν. *Case a* (Table 4a) assigns broad layer-dependent ranges to V_s and V_p, while treating density and Poisson's ratio as depth-invariant across the whole profile. Overall, the admissible ranges span V_s = 90–3000 m/s and V_p = 200–5000 m/s, while ρ is allowed to vary globally within 1600–3000 kg/m^3 and ν within 0.20–0.40. The layer interface depths are only weakly constrained, with the bottom depth of Layer 1 in 0.2–0.3 m, of Layer 2 in 0.4–0.6 m, and of Layer 3 in 0.9–1.1 m, while Layer 4 is modeled as a half-space. *Case b* (Table 4b) retains the same four-layer scheme and the same overall bounds for wave velocities, i.e., V_s = 90–3000 m/s and V_p = 200–5000 m/s, as well as the same interface-depth ranges (z_1 = 0.2–0.3 m, z_2 = 0.4–0.6 m, z_3 = 0.9–1.1 m). Compared with Case a, it introduces tighter density constraints: overall, ρ is bounded between 1600 and 2600 kg/m^3, with a higher, layer-specific range prescribed for the reinforced-concrete invert (Layer 3: 2300–2600 kg/m^3), whereas the remaining layers share 1600–2100 kg/m^3. Poisson's ratio remains depth-invariant with global bounds 0.20–0.40. Finally, *Case c* (Table 4c) is the most constrained and physically informed. It preserves the same overall bounds for V_s and V_p (V_s = 90–3000 m/s and V_p = 200–5000 m/s) and the same interface-depth ranges (z_1 = 0.2–0.3 m, z_2 = 0.4–0.6 m, z_3 = 0.9–1.1 m). Density bounds follow Case b, i.e., overall ρ = 1600–2600 kg/m^3 with a higher range for Layer 3. In addition, Poisson's ratio is allowed to vary by layer to reflect the expected contrast between granular ballast and concrete: overall ν spans 0.15–0.40, with Layer 3 constrained to 0.15–0.25, while the other layers retain 0.20–0.40. Overall, the transition from Case a (Table 4a) to Case c (Table 4c) represents an intentional increase in prior constraints to stabilize the inversion and to limit parameter coupling among V_s, V_p, ρ, and thickness.

Fig. 8 summarizes the best-fit inverted profiles for all six inversions, while Table 5 reports the corresponding best-fit layered models (including V_s, V_p, ρ, and layer thickness). The variability of the inversion outcomes is illustrated by the ensemble of the 1000 best-fitting layered profiles for each case (Fig. 9) and by the corresponding set of

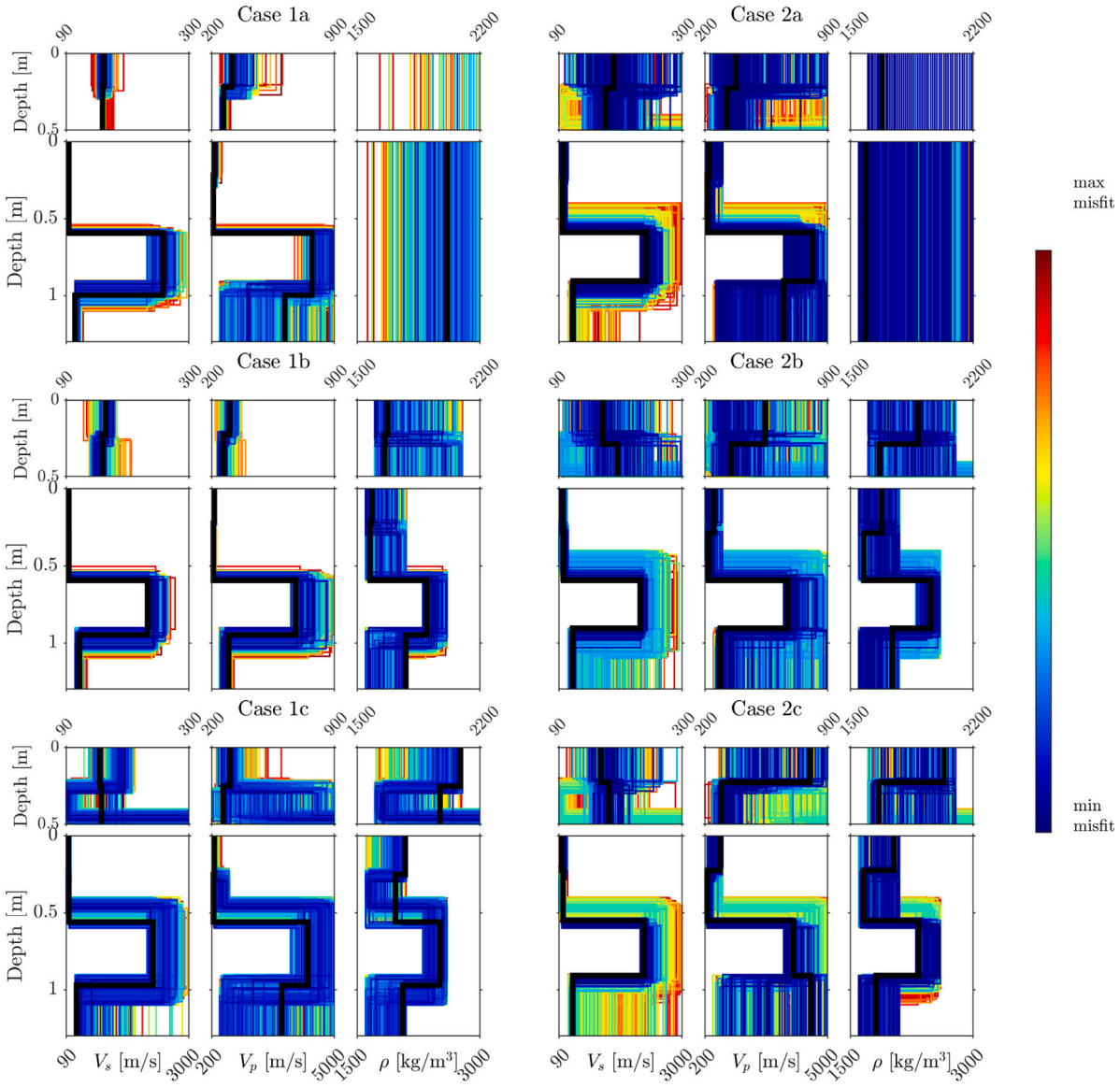

Fig. 9. Best 1000 layered profiles obtained from MASW inversion for all cases. The best profile, with lowest misfit, is indicated with the solid black line. A zoomed view, on top of each profile, is included to detail ballast layers.

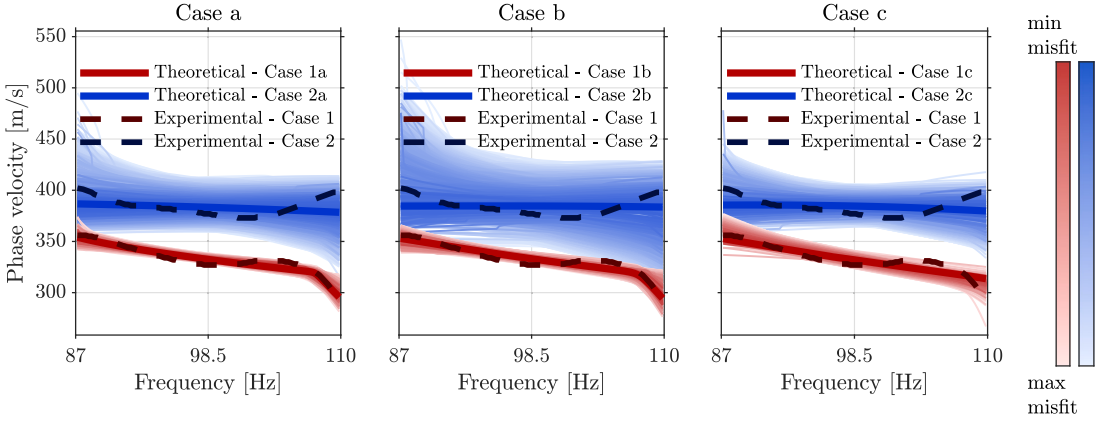

Fig. 10. Dispersion-curve variability for the six inversions. For each case, the 1000 best-fitting theoretical fundamental-mode Rayleigh-wave dispersion curves returned by the inversion are plotted; darker shades indicate lower misfit, with the darkest curve corresponding to the overall best-fit model. The experimentally picked dispersion curves extracted from the phase-shift image are superimposed for reference.

the 1000 best-fitting theoretical dispersion curves compared with the experimentally picked curves (Fig. 10).

Despite the differences in parameterization, the obtained results confirm that the Rayleigh-wave dispersion curve is primarily controlled by the V_s structure, whereas it is only weakly sensitive to V_p and ρ over the investigated frequency band, as already observed in the literature [30,37]. This behavior is reflected in the inversion outputs: within each case, the best-fitting models yield a stable and repeatable V_s stratigraphy, while V_p and ρ show larger admissible variability (Fig. 8). This contrast is even clearer when inspecting the ensemble of the 1000 best-fitting layered profiles (Fig. 9), where the spread of acceptable solutions is markedly larger for V_p and ρ than for V_s. The same plots also indicate that the variability of acceptable models tends to increase when moving towards the more constrained parameterizations, and it is generally more pronounced for the fastened-rail configurations, with an increase in variability also affecting V_s.

At the same time, the dispersion-curve ensembles (Fig. 10) show that the 1000 best models of each case reproduce the experimentally picked curve reasonably well over the selected frequency band, consistently with the underlying dispersion image used for picking. A systematic difference is nevertheless observed between track configurations: the unfastened-rail cases exhibit a tighter cluster of theoretical dispersion curves and a closer match to the picked experimental curve, whereas the fastened-rail cases show a poorer overall match accompanied by a broader spread of acceptable theoretical curves.

Since the dispersion curve is predominantly controlled by the V_s structure, we use MASW here primarily to estimate ballast-scale V_s profiles robustly. Where needed, small-strain stiffness is then derived through Eq. (1) using representative density values supported by the laboratory benchmark and by physically plausible bounds.

For rails unfastened (Cases 1a–1c), the inversion consistently resolves a two-layer ballast structure, comprising a first ballast layer (Layer 1; $V_s \approx$ 148–157 m/s) over a second deeper ballast layer (Layer 2; $V_s \approx$ 151–153 m/s). The associated thicknesses are stable across parameterizations (Table 5), with Layer 1 spanning 0.22–0.25 m and Layer 2 spanning 0.31–0.37 m, yielding a total ballast thickness of about 0.56–0.59 m, consistent with expectations for the investigated section. The reinforced-concrete invert is expressed as a very high-velocity layer (Layer 3; $V_s \approx$ 2016–2381 m/s) with thickness 0.35–0.41 m. Beneath the invert, the soil half-space exhibits $V_s \approx$ 303–413 m/s (Layer 4), consistent with the V_s value of about 380 m/s reported from geophysical investigations performed in the same urban area [38]. The corresponding best-fit V_p values in the ballast range from ~304 to 316 m/s in Layer 1 and from ~264 to 270 m/s in Layer 2, while the concrete layer reaches several km/s ($V_p \approx$ 3.47–4.11 km/s), consistent with a stiff structural material. As expected, density is comparatively less stable across Cases 1a–1c (Table 5), reflecting the weak sensitivity of Rayleigh-wave phase-velocity data to ρ over the investigated frequency band. The achieved misfits for the unfastened configuration were 0.0125 (Case 1a), 0.0137 (Case 1b), and 0.0181 (Case 1c).

For rails fastened (Cases 2a–2c), the same four-layer structure is retrieved, but the ballast portion of the profile appears systematically stiffer. The first ballast layer (Layer 1) increases to $V_s \approx$ 162–182 m/s, with thickness 0.23–0.29 m, while the second ballast layer (Layer 2) falls in the range $V_s \approx$ 169–190 m/s, with thickness 0.31–0.36 m, yielding a total ballast thickness of about 0.56–0.60 m. The reinforced-concrete invert remains associated with very high velocities ($V_s \approx$ 2000–2143 m/s) and a thickness of 0.31–0.36 m, while the underlying soil half-space is retrieved with $V_s \approx$ 404–421 m/s (Layer 4). Best-fit V_p values are again low in the ballast layers (approximately 300–800 m/s in Layer 1 and ~295–349 m/s in Layer 2), increase to several km/s in the concrete layer (~3.43–4.40 km/s), and show larger variability in the half-space (Table 5). The misfits for the fastened configuration were slightly higher but mutually consistent across parameterizations: 0.0218 (Case 2a), 0.0221 (Case 2b), and 0.0226 (Case 2c).

The systematic increase in ballast V_s for fastened rails is consistent with the dispersion images, where the dominant band between 80 and 120 Hz exhibits higher phase velocities for the fastened configuration. This behavior is compatible with residual rail-guided energy and a stronger structural influence of the rail-sleeper system on the measured wavefield, which may bias the apparent Rayleigh-wave phase velocity towards higher values.

In summary, exploring progressively constrained parameterizations (Cases a–c) confirms that (i) the inverted V_s stratigraphy is robust and only weakly affected by the treatment of V_p, ρ and ν, which instead exhibit larger admissible variability, and (ii) the comparison between rails unfastened and fastened provides clear evidence that unfastening is important to obtain reliable ballast-scale V_s values from active MASW in the tunnel environment.

Discussion of the experimental outcomes

This work combines a controlled laboratory reference dataset with an in-situ active MASW survey carried out inside a metro tunnel, and, crucially, repeats the field acquisition under two track boundary conditions (rails unfastened vs. fastened). The discussion therefore focuses on (i) the interpretation of the unfastened/fastened comparison, (ii) what can be considered robust given the tested inversion parameterizations, and (iii) the consistency between laboratory and field results, with implications for the likely ballast state.

The paired unfastened/fastened comparison provides direct evidence that the rail-sleeper system can influence the measured wavefield and therefore bias the dispersion image when the goal is to characterize the ballast alone. Although both dispersion images show a dominant continuous band between 80 and 120 Hz (Figs. 6(c) and 6(d)), the fastened case systematically exhibits energy ridges at higher phase velocities in the same band. In a Rayleigh-wave framework, a systematic shift towards higher phase velocity generally maps to a stiffer equivalent near-surface medium over the wavelengths sampled [39]; consistently, the inversions for the fastened rails case yield higher shallow V_s values than the unfastened rails inversion cases (Fig. 8 and Table 5). For the unfastened cases (1a–1c), the shallow ballast sublayer (Layer 1) remains within $V_s \approx$ 148–157 m/s, whereas for the fastened cases (2a–2c) it increases to $V_s \approx$ 162–182 m/s. The deeper ballast interval (Layer 2) is also affected: $V_s \approx$ 151–153 m/s in the unfastened configuration and $V_s \approx$ 169–190 m/s in the fastened configuration. This systematic stiffening of the shallowest part of the profile when rails are fastened is compatible with residual rail-guided energy and stronger coupling of the measured wavefield to the track structure, whereby a portion of the recorded energy is controlled by the rail-sleeper system rather than by the ballast-invert-soil continuum alone. In addition, the two configurations likely differ in the stress state imposed on the ballast during acquisition. When rails are fastened, the rail load is transferred to the ballast through the sleeper system in its standard configuration, promoting a relatively uniform support condition along the track. Conversely, when rails are unfastened and slightly lifted on wooden strips, the rail support may become more localized at discrete contact points, potentially inducing stress concentrations and a different confinement pattern in the shallow ballast. This effect could contribute to differences in the inferred small-strain stiffness, since the laboratory benchmark (Section “Laboratory reference dataset”) clearly shows that ballast shear-wave velocity V_s is strongly stress-dependent (Table 3). However, stress localization contribution is expected to be limited in the unfastened setup, because the wooden supports were located outside the receiver aperture. In operational terms, this comparison supports a clear recommendation emerging from the campaign: unfastening the running rails is important when the purpose of the survey is to retrieve the shear-wave velocity V_s at the ballast-scale within a constrained tunnel environment and with a relatively short array. The misfit values provide a consistent additional indicator. The unfastened inversions yield smaller misfits (1.24×10^{-2} to 1.80×10^{-2})

than the fastened inversions (2.18×10^{-2} to 2.25×10^{-2}). All misfits remain acceptable given the restricted frequency band and picking uncertainty, but the systematic increase for the fastened configuration suggests that the measured wavefield departs more from the assumptions underlying 1-D Rayleigh-wave inversion (laterally homogeneous layering and dominance of the fundamental surface-wave mode). A plausible interpretation is that the fastened case contains a stronger mixture of track-structural and ground-controlled components, which is more difficult to represent with the adopted 1-D layered model class.

The three tested parameterizations (Cases a–c; Table 4) were intentionally designed to progressively increase prior constraints. Two outcomes are important for interpretation. Firstly, within each rail configuration, the recovered V_s layering is comparatively stable across Cases a–c: the shallow-ballast V_s and the overall stiffness gradient with depth remain consistent, while V_p and especially ρ vary more among best-fit solutions (Table 5). This is fully consistent with the known sensitivity structure of Rayleigh-wave dispersion, which is primarily controlled by V_s and layer thicknesses, and only weakly sensitive to V_p and ρ over the investigated band. In practical terms, the parameterization affects the admissible solution space and model plausibility checks, but the dispersion data themselves strongly constrain the V_s structure required to fit the picks. Secondly, the variability of ρ across best-fit models reinforces that any absolute estimate of G_0 (through Eq. (1)) from MASW alone should be treated with caution unless density is constrained independently. This is precisely where the laboratory benchmark becomes essential: it provides realistic stiffness ranges for ballast under controlled confinement and degradation mechanisms and therefore supports physically plausible bounds for both V_s and representative ρ values used in G_0 estimation.

The inverted stratigraphy is also interpretable against the expected tunnel-track geometry. The design drawings indicate a ballast thickness of about 0.5 m over a reinforced-concrete invert, followed by subgrade soil, and these interfaces are marked in Fig. 8. Across all cases, the inversion retrieves two ballast sublayers within the upper ~0.56–0.60 m, which is consistent with the expected order of magnitude for the ballast thickness in the investigated section (Table 5). Below the ballast, a very high-V_s layer is consistently recovered and is naturally associated with the reinforced-concrete invert. Some variability is observed in the inferred invert thickness and velocity, which is consistent with the limited wavelength coverage and the difficulty of resolving a relatively thin, high-contrast layer at the edge of the available resolution. Beneath the invert, the soil half-space is retrieved with V_s values that are systematically higher than ballast, as expected for a stiffer supporting ground, but lower than the reinforced-concrete invert (Table 5).

It should be noted that the laboratory benchmark and the field survey were not performed on exactly the same ballast material. The ballast in the tunnel is andesite, whereas the laboratory tests were carried out on basalt ballast. Both materials are hard igneous rocks commonly used for railway ballast. Available data on ballast selection show that basalt and andesite have comparable abrasion and crushing properties and that both generally satisfy ballast quality requirements [40]. However, differences in rock type, mineral composition, particle shape, quarrying conditions, and weathering may affect degradation processes and stiffness evolution. For this reason, the laboratory dataset is used here to check the plausibility of the field results and to support the interpretation of the inversion, rather than to represent the exact response of the andesite ballast tested in the tunnel. The laboratory benchmark provides a useful reference frame to interpret the plausibility of the in-situ ballast-scale V_s values. In particular, the laboratory results (Table 3) show that ballast V_s is strongly stress-dependent and varies markedly with degradation state. For comparison with the shallowest in-situ ballast, the most relevant laboratory condition is Phase F, corresponding to $\sigma_v = 0$ kPa, which is closer to the low confinement expected near the ballast surface. Under Phase F, fresh ballast (FB) and fresh-fouled ballast (FFB) exhibit $V_s \approx 148$ and 141 m/s, respectively, whereas the abraded conditions yield higher values (AB: ~210 m/s; AFB: ~160 m/s). The unfastened-case inversions return V_s values for the first ballast layer (Layer 1) in the range ~148–157 m/s, which is consistent with the Phase F laboratory values for fresh ballast and with the visual observation of clean ballast at the surface. In contrast, the fastened inversions yield higher Layer 1 velocities ($V_s \approx 162$–182 m/s), which overlap the AFB range at Phase F and trend towards the lower bound of the AB response, suggesting an unrealistically stiff surface ballast.

For the second deeper ballast layer, the most appropriate laboratory reference is given by the phases at $\sigma_v = 10$ kPa (C1 and CSS1–CSS4), which represent a more confined state than the surface and are closer to the stress conditions expected at depth. In situ, however, the effective vertical stress in this depth range is still limited: for typical ballast bulk densities (e.g., $\rho \approx 1700$ kg/m^3), the overburden over 0.3–0.6 m corresponds to about 5–10 kPa, i.e., comparable to or lower than the laboratory confinement level. Over these 10 kPa laboratory phases, V_s values generally increase (Table 3), with fresh ballast (FB) typically in the ~185–206 m/s range during CSS phases, while AB/AFB and FFB often exceed 200 m/s. Against this reference, the unfastened Layer 2 values ($V_s \approx 151$–153 m/s) remain comparatively low, which is consistent with a lower in-situ confinement than 10 kPa and with the fact that Rayleigh-wave inversion returns an effective, wavelength-averaged stiffness over the sampled depth interval. Conversely, the fastened Layer 2 values ($V_s \approx 169$–190 m/s) lie closer to the lower bound of the 10 kPa laboratory range for fresh ballast.

Finally, the laboratory dataset strengthens the plausibility of the unfastened inversion and provides a reference frame to interpret the field profile as representative of a reasonably healthy ballast bed, within the limits imposed by unknown in-situ degradation state and by material and tensional state differences.

The present study provides a single time characterization of the investigated track section, rather than a complete Structural Health Monitoring (SHM) application. Nevertheless, the same measurement and inversion workflow could be potentially repeated over time on selected tunnel sections to follow the evolution of ballast scale V_s. Periodic surveys could be performed before and after maintenance operations, such as tamping, or at fixed time intervals in sections affected by recurrent geometry defects, transition zones, or high vibration levels. In this way, changes in the dispersion image and retrieved V_s profiles could be used as indicators of stiffness variation, ballast degradation, or loss of support. However, this potential use would require further investigation through repeated surveys on the same track sections and comparison with independent information on ballast condition.

From an operational perspective, rail unfastening increases the effort required for the survey. In the present campaign, approximately 30 min were needed to unfasten and lift the rails, and a similar time was required to restore the fastened configuration. The procedure also required dedicated tools and trained operators. Therefore, rail unfastening is not proposed as a routine procedure for extensive surveys along long tunnel sections. Rather, it should be regarded as a high fidelity diagnostic option for selected locations where a ballast representative stiffness estimate is particularly important. If the rails are kept fastened, the survey is operationally simpler, but the present results indicate systematically higher apparent ballast shear-wave velocities, with increases of about 10%–25% for the tested parameterizations. In this case, the fastened configuration should be interpreted as representative of the coupled track and ballast response, rather than as a direct estimate of ballast stiffness alone.

Overall, the discussion supports three main conclusions. Firstly, the paired measurements demonstrate that unfastening the rails is important to reduce rail-guided and rail-sleeper coupling effects and to obtain ballast-representative dispersion images in tunnel conditions, as also reflected by the tighter dispersion-curve ensembles and lower misfits in the unfastened cases. Secondly, the inversion results are robust with respect to the tested parameterizations in terms of the retrieved V_s layering, while V_p and ρ remain comparatively less constrained and more

variable across acceptable solutions, as expected from Rayleigh-wave dispersion sensitivity. Thirdly, the laboratory benchmark indicates that, in the unfastened case, Layer 1 V_s values are consistent with a low-confinement fresh ballast response; the second deeper ballast layer exhibits comparable V_s values rather than a pronounced increase, which is compatible with an in-situ stress state lower than the 10 kPa laboratory reference and with the uncertainty in ballast degradation state.

Conclusions

This paper presented an active MASW campaign performed inside an operational metro tunnel (Milan Metro Line M1) to retrieve ballast-scale shear-wave velocity profiles under severe geometric and operational constraints. To our knowledge, this is the first documented application of *active* MASW executed inside a metro tunnel and explicitly designed to quantify the influence of track boundary conditions on dispersion imaging and inversion.

Three main conclusions can be drawn.

1. **Active MASW is feasible in a tunnel and can resolve ballast-scale stiffness trends.** A compact, densely sampled array (0.32 m spacing over 3.84 m aperture) provided a stable continuous dispersion band (87–110 Hz) suitable for inversion. The inverted profiles consistently resolved two ballast sublayers over a stiff reinforced-concrete invert and an underlying soil half-space, in agreement with the expected tunnel-track stratigraphy and within the resolution limits imposed by the acquisition geometry.
2. **Track boundary conditions matter: rail unfastening is critical for ballast-representative results.** Repeating the survey with rails fastened and unfastened showed that the fastened configuration yields systematically higher phase velocities within the dominant dispersion band and correspondingly higher V_s values for the ballast layers. This behavior is consistent with a stronger structural influence of the rail-sleeper system and residual rail-guided energy in the measured wavefield. The unfastened configuration produced lower misfits and more plausible shallow stiffness values, indicating that rail unfastening is an important practical step to mitigate bias and to obtain dispersion images representative of the ballast-invert-soil system. This does not imply that the fastened case results are unusable; rather, it suggests that they are more likely to represent the operational, coupled track–ground system response, while the unfastened configuration better reflects the layered ballast-invert-subgrade system targeted by the survey.
3. **Inversion outcomes confirm that V_s is robust, while V_p and ρ remain weakly constrained; laboratory data are essential for interpretation.** Testing three progressively constrained parameterizations (Cases a–c) demonstrated that the inferred V_s layering is stable across reasonable choices of V_p, ρ and ν, consistent with the known sensitivity of Rayleigh-wave dispersion. Conversely, density remained comparatively non-unique, implying that absolute G_0 estimates should rely on independent density information. The laboratory benchmark, which documents the strong stress and degradation dependence of ballast V_s, provided critical context to interpret the in-situ profiles and supported the plausibility of the unfastened results as representative of clean, lightly confined ballast near the surface.

Overall, the study outlines an operational workflow for tunnel-deployable active MASW and highlights a key methodological requirement (controlling rail boundary conditions) to achieve ballast-representative stiffness profiles. Future work should extend the procedure to multiple tunnel sections where ballast condition is independently documented (gradation, fouling level, moisture and density), so that spatial variability and degradation trends can be quantitatively linked to the retrieved V_s profiles.

CRediT authorship contribution statement

Valerio Maugeri: Writing – original draft, Visualization, Software, Methodology, Investigation, Formal analysis, Conceptualization. **Luca Martinelli:** Writing – review & editing, Supervision, Methodology, Conceptualization. **Marco Acquati:** Writing – review & editing, Resources, Conceptualization. **Cristina Jommi:** Writing – review & editing, Supervision, Methodology, Investigation, Conceptualization.

Funding

This research was performed within the framework of the service contract between Politecnico di Milano and MM S.p.A. No additional external funding was received for this study.

Declaration of competing interest

The authors declare that they have no known competing financial interests or personal relationships that could have appeared to influence the work reported in this paper.

Acknowledgments

The authors acknowledge ATM S.p.A. for granting access to the Milan Metro infrastructure and for the operational support provided during the field campaign. The geophysical measurements were carried out by Tecno In S.r.l., whose technical expertise and on-site assistance are warmly acknowledged.

Data availability

The data that support the findings of this study are not publicly available because they relate to measurements performed in an operational underground railway infrastructure and are subject to confidentiality and access restrictions. Data may be made available from the corresponding author upon reasonable request and subject to approval by the relevant infrastructure owners.

References

[1] Nelson JT, Saurenman HJ. A prediction procedure for rail transportation groundborne noise and vibration. Transp Res Rec 1987;1143:26–35, URL: https://onlinepubs.trb.org/Onlinepubs/trr/1987/1143/1143-005.pdf.

[2] Degrande G, Clouteau D, Othman R, Arnst M, Chebli H, Klein R, Chatterjee P, Janssens B. A numerical model for ground-borne vibrations from underground railway traffic based on a periodic finite element–boundary element formulation. J Sound Vib 2006;293(3):645–66. http://dx.doi.org/10.1016/j.jsv.2005.12.023.

[3] Charoenwong C, Connolly DP, Alves Costa P, Galvín P, Romero A, Wang T, Liu K. The effect of ballast moisture content and fouling index on railway track settlement. Transp Geotech 2024;45:101193. http://dx.doi.org/10.1016/j.trgeo.2024.101193.

[4] Chen J, Vinod JS, Indraratna B, Ngo NT, Gao R, Liu Y. A discrete element study on the deformation and degradation of coal-fouled ballast. Acta Geotech 2022;17:3977–93. http://dx.doi.org/10.1007/s11440-022-01453-4.

[5] Koohmishi M, Azarhoosh A. Stiffness and damping properties of railway ballast aggregate considering influence of degradation of aggregate and incorporation of crumb rubber. Soil Dyn Earthq Eng 2022;155:107177. http://dx.doi.org/10.1016/j.soildyn.2022.107177.

[6] Liu G, Cong J, Wang P, Du S, Wang L, Chen R. Study on vertical vibration and transmission characteristics of railway ballast using impact hammer test. Constr Build Mater 2022;316:125898. http://dx.doi.org/10.1016/j.conbuildmat.2021.125898.

[7] Milne D, Harkness J, Le Pen L, Powrie W. The influence of variation in track level and support system stiffness over longer lengths of track for track performance and vehicle track interaction. Veh Syst Dyn 2021;59(2):245–68. http://dx.doi.org/10.1080/00423114.2019.1677920.

[8] Zuada Coelho B. Influence of railway track degradation on vibration generation. Technical Report, Deltares; 2023, URL: https://www.prorail.nl/siteassets/homepage/programmas/innovatieagenda-bronaanpak-spoortrillingen/kennisdocumenten/2a-obo/influence-of-railway-track-degradation-on-vibration-generation.pdf.

[9] Guo Y, Markine V, Jing G. Review of ballast track tamping: Mechanism, challenges and solutions. Constr Build Mater 2021;300:123940. http://dx.doi.org/10.1016/j.conbuildmat.2021.123940.
[10] Charoenwong C, Connolly DP, Wang T, Liu K, Alves Costa P, Romero A, Galvín P. Prediction of future railway ballast tamping requirements. Transp Geotech 2025;55:101652. http://dx.doi.org/10.1016/j.trgeo.2025.101652.
[11] Anderson W, Fair P. Behavior of railway ballast under monotonic and cyclic loading conditions. J Geotech Geoenviron Eng 2008;134(3):289–99. http://dx.doi.org/10.1061/(ASCE)1090-0241(2008)134:3(316).
[12] Suiker ASJ, Selig ET, Frenkel R. Static and cyclic triaxial testing of ballast and subballast. J Geotech Geoenvironmental Eng 2005;131(6):771–82. http://dx.doi.org/10.1061/(ASCE)1090-0241(2005)131:6(771).
[13] Lackenby J, Indraratna B, McDowell G, Christie D. Effect of confining pressure on ballast degradation and deformation under cyclic triaxial loading. Géotechnique 2007;57(6):527–36. http://dx.doi.org/10.1680/geot.2007.57.6.527.
[14] Indraratna B, Ionescu D, Christie HD. Shear behavior of railway ballast based on large-scale triaxial tests. J Geotech Geoenvironmental Eng 1998;124(5):375–466. http://dx.doi.org/10.1061/(ASCE)1090-0241(1998)124:5(439).
[15] Indraratna B, Tennakoon NC, Nimbalkar SS, Rujikiatkamjorn C. Behavior of clay fouled ballast under drained triaxial testing. Géotechnique 2013;63(5):410–9. http://dx.doi.org/10.1680/geot.11.P.086.
[16] Park CB, Miller RD, Xia J, Ivanov J. Multichannel analysis of surface waves (MASW)—active and passive methods. Lead Edge 2007;26(1):60–4. http://dx.doi.org/10.1190/1.2431832.
[17] Anbazhagan P, Indraratna B, Rujikiatkamjorn C, Su L. Using a seismic survey to measure the shear modulus of clean and fouled ballast. Geomech Geoengin 2010;5(2):117–26. http://dx.doi.org/10.1080/17486020903497431.
[18] Anbazhagan P, Indraratna B, Amarajeevi G. Characterization of clean and fouled rail track ballast subsurface using seismic surface survey method: model and field studies. J Test Eval 2011;39(5):831–41. http://dx.doi.org/10.1520/JTE103472.
[19] Hwang HJ, Park HC. Evaluation of condition of gravel ballast layer on high-speed railway using surface wave method based on harmonic wavelet analysis of waves. NDT E Int 2014;68:78–87. http://dx.doi.org/10.1016/j.ndteint.2014.08.005.
[20] De Bold R, Connolly DP, Patience S, Lim M, Forde MC. Using impulse response testing to examine ballast fouling of a railway trackbed. Constr Build Mater 2021;274:121888. http://dx.doi.org/10.1016/j.conbuildmat.2020.121888.
[21] Kang M, Wang H, Qamhia IIA, Tutumluer E, Haddani Y, Bankston A. Degraded ballast stiffness characterization using bender element field sensor and PANDA® penetrometer. Transp Res Rec 2023;2677(8):428–38. http://dx.doi.org/10.1177/03611981231156936.
[22] Dai K, Liu K, Li X, You Q, Tang H, Xu Q. Application of passive multichannel analysis of surface waves method at sites close to underground railways - Problems and a case study. J Appl Geophys 2019;164:191–9. http://dx.doi.org/10.1016/j.jappgeo.2019.03.009.
[23] Trinh VN, Tang AM, Cui YJ, Dupla JC, Canou J, Calon N, Lambert L, Robinet A, Schoen O. Mechanical characterisation of the fouled ballast in ancient railway track substructure by large-scale triaxial tests. Soils Found 2012;52(3):511–23. http://dx.doi.org/10.1016/j.sandf.2012.05.009.
[24] Lin PS, Chang CW, Chang WJ. Characterization of liquefaction resistance in gravelly soil: Large hammer penetration test and shear wave velocity approach. Soil Dyn Earthq Eng 2004;24(9):675–87. http://dx.doi.org/10.1016/j.soildyn.2004.06.010.
[25] Al-Mashhor AA, Al-Shuhail AA, Hanafy SM, Mousa WA. First arrival picking of seismic data based on trace envelope. IEEE Access 2019;7:128806–15. http://dx.doi.org/10.1109/ACCESS.2019.2939320.
[26] Foti S, Hollender F, Garofalo F, Albarello D, Asten M, Bard PY, Comina C, Cornou C, Cox B, Di Giulio G, Forbriger T, Hayashi K, Lunedei E, Martin A, Mercerat D, Ohrnberger M, Poggi V, Renalier F, Sicilia D, Socco V. Guidelines for the good practice of surface wave analysis: a product of the InterPACIFIC project. Bull Earthq Eng 2018;16:2367–420. http://dx.doi.org/10.1007/s10518-017-0206-7.
[27] O'Neill A, Dentith M, List R. Full-waveform P-SV reflectivity inversion of surface waves for shallow engineering applications. Explor Geophys 2003;34(3):158–73. http://dx.doi.org/10.1071/EG03158.
[28] Taipodia J, Dey A, Baglari D. Influence of data acquisition and signal preprocessing parameters on the resolution of dispersion image from active MASW survey. J Geophys Eng 2018;15(4):1310–26. http://dx.doi.org/10.1088/1742-2140/aaaf4c.
[29] Park CB. SurfSeis: Active and passive MASW (supplementary) user's manual, version 2.0. In: Adkins-Heljeson M, editor. Lawrence, Kansas: Kansas Geological Survey; 2006, Revised by Julian Ivanov and Mary Brohammer (Jan 2007).
[30] Socco LV, Strobbia C. Surface-wave method for near-surface characterization: a tutorial. Near Surf Geophys 2004;2(4):165–85. http://dx.doi.org/10.3997/1873-0604.2004015.
[31] Wathelet M, Chatelain J, Cornou C, Di Giulio G, Guillier B, Ohrnberger M, Savvaidis A. Geopsy: A user-friendly open-source tool set for ambient vibration processing. Seismol Res Lett 2020;91(3):1878–89. http://dx.doi.org/10.1785/0220190360.
[32] Park CB, Miller RD, Xia J. Imaging dispersion curves of surface waves on multichannel record. In: SEG technical program expanded abstracts. 1998, p. 1377–80. http://dx.doi.org/10.1190/1.1820161.
[33] Park CB, Miller RD, Xia J. Multichannel analysis of surface waves. Geophysics 1999;64(3):800–8. http://dx.doi.org/10.1190/1.1444590.
[34] McMechan GA, Yedlin MJ. Analysis of dispersive waves by wave field transformation. Geophysics 1981;46(6):869–74. http://dx.doi.org/10.1190/1.1441225.
[35] Wathelet M, Jongmans D, Ohrnberger M. Surface-wave inversion using a direct search algorithm and its application to ambient vibration measurements. Near Surf Geophys 2004;2(4):211–21. http://dx.doi.org/10.3997/1873-0604.2004018.
[36] Wathelet M. An improved neighborhood algorithm: Parameter conditions and dynamic scaling. Geophys Res Lett 2008;35:L09301. http://dx.doi.org/10.1029/2008GL033256.
[37] Pan L, Chen X, Wang J, Yang Z, Zhang D. Sensitivity analysis of dispersion curves of Rayleigh waves with fundamental and higher modes. Geophys J Int 2019;216:1276–303. http://dx.doi.org/10.1093/gji/ggy479.
[38] Pontani N, Martinelli L, Acquati M, Jommi C. A numerical assessment of variable saturation of the upper layers on the ground borne vibrations from underground trains: A case history. Transp Geotech 2023;40:100981. http://dx.doi.org/10.1016/j.trgeo.2023.100981.
[39] Xia J, Miller RD, Park CB. Estimation of near-surface shear-wave velocity by inversion of Rayleigh waves. Geophysics 1999;64(3):691–700. http://dx.doi.org/10.1190/1.1444578.
[40] Guo Y, Xie J, Fan Z, Markine V, Connolly DP, Jing G. Railway ballast material selection and evaluation: A review. Constr Build Mater 2022;344:128218. http://dx.doi.org/10.1016/j.conbuildmat.2022.128218.